A numerical study on the mixing of air and hydrogen in a scramjet combustor

M. Ali
Department of Mechanical Engineering,
University of Engineering and Technology (BUET)
Dhaka, Bangladesh

T. Fujiwara
Department of Aerospace Engineering
Nagoya University, Nagoya, Japan

ABSTRACT

A numerical study on mixing of air and hydrogen is performed by solving two-dimensional full Navier-Stokes equations. The main stream is air of Mach 5 entering through the configured inlet of the combustor and gaseous hydrogen is injected from the configured jet on the side wall. Supersonic mixing and diffusion mechanisms of a transverse hydrogen jet in two-dimensional finite air streams have been analyzed and discussed. The computed results are compared with the experimental data and show good agreement. For an otherwise fixed combustor geometry, the air inlet width and injection angle are varied to study the physics of mixing and flow field characteristics. On the effect of inlet width variation, two competing phenomena have been observed: (i) upstream of injector the strength of recirculation is higher for wider inlet and consequently the mixing increases, and (ii) downstream, the diffusion of hydrogen decreases with the increase of inlet width and eventually mixing decreases. As a result, in far downstream the mixing efficiency increases up to certain inlet width and then decreases for further increment of inlet width. For the variation of injection angle results show that upstream of injector the mixing is dominated by recirculation and downstream the mixing is dominated by mass concentration of hydrogen. Upstream recirculation is dominant for injecting angle 60° and 90°. Incorporating the various effects, perpendicular injection shows the maximum mixing efficiency and its large upstream recirculation region has a good flame holding capability.

NOMENCLATURE

b	air inlet width	mm
c	sound speed	m/s
C_p	specific heat at constant pressure	J/(kg.K)
D_t	turbulent diffusion coefficient	m^2/s
E	total energy	J/m^3
$\mathbf{F}$	flux vector in x-direction	
$\hat{\mathbf{F}}$	transformed flux vector in ξ-direction	
$\mathbf{G}$	flux vector in y-direction	
$\hat{\mathbf{G}}$	transformed flux vector in η-direction	
H	enthalpy	J/kg
J	transformation Jacobian	
m	mass flux of species	kg/s
p	pressure	Pa
q	energy flux by conduction	W/m^2
R	universal gas constant	J/(kg.mol.K)
T	temperature	K
u	horizontal velocity	m/s
u_e	velocity at the edge of boundary layer	m
$\mathbf{U}$	vector of conservative variables	
$\hat{\mathbf{U}}$	transformed vector of conservative variables	
U	contravariant velocity in ξ-direction	
v	vertical velocity	m/s
V	contravariant velocity in η-direction	
W	molecular weight of species	gm/mol
x	horizontal cartesian co-ordinate	m
Y	mass fraction of species	
y	vertical cartesian co-ordinate	m
z	mole fraction of species	

Greek symbols

θ	injecting angle	
ξ	transformed co-ordinate in horizontal direction	
η	transformed co-ordinate in vertical direction	
ρ	mass density	kg/m^3
σ	normal stress	Pa
τ	shear stress	Pa

Paper No. 2911 Manuscript received on 31 August 2004, revised version received 18 March 2005, Approved 26 April 2005.

https://doi.org/10.1017/S0001924000000774 Published online by Cambridge University Press

μ	coefficient of dynamic viscosity	kg/(m.s)
κ	thermal conductivity	W/(m.K)
δ	boundary layer thickness	m
δ^*	Kinematic displacement thickness	m
ϕ'	local equivalence ratio of hydrogen and oxygen	
Φ	global equivalence ratio of hydrogen and oxygen	
φ	contour level	

Superscripts

ns	number of species

Subscripts

i,j	index for species
l	laminar case
m	mixture
t	index for turbulence
v	viscosity term
x	horizontal direction
y	vertical direction
xy	reference plane
0	reference value, stagnation condition

Keywords

Scramjet engine, TVD scheme, Backward-facing step, Supersonic mixing.

1.0 INTRODUCTION

Mixing of fuel with oxidizer and their combustion are encountered in many engineering applications including hypersonic propulsion systems in space vehicles. Particularly, the fuel injection scheme in hypersonic vehicles incorporating Scramjet (supersonic combustion ramjet) engines, requires special attention for efficient mixing and stable combustion. Though some of the researches have been carried out on mixing and combustion of fuel with oxidizer in Scramjet programmes, still it faces many unresolved problems. The main problems that arise in this regard concern mixing of reactants, ignition, flame holding, and completion of combustion. More investigations are required to overcome these problems. In fact, in supersonic combustion, high penetration and mixing of injectant with main stream is difficult due to their short residence time in combustor as described by Brown *et al*[1] and Papamoschou *et al*[2]. These investigations showed that good mixing and high penetration of injectant is difficult for the flow of high Mach number. Therefore, it is necessary to investigate the physical mechanisms that affect the mixing and combustion in Scramjet engine.

Several investigations have been performed to analyze the mixing and combustion characteristics, and find out the means of increasing the mixing efficiency. In these investigations the authors showed a number of parameters that can affect penetration and mixing. In an experiment, Rogers[3] showed the effect of the ratio between jet dynamic pressure and freestream dynamic pressure on the penetration and mixing of a sonic hydrogen jet injected normal to a Mach 4 airstream. In similar flow arrangements, Kraemer *et al*[4] found that the relative change in jet momentum was directly proportional to the relative size between the flow field disturbance and the upstream separation distance. A typical jet flow field and several associated terms of upstream separated flow are shown in Fig. 1. The flow field disturbances were created by the jet injected from side wall. By using different pressures and widths of jet and gas samples the momentum and eventually the flow field disturbances were changed. The distance in upstream of jet at which the separation of flow occurred, was referred to as the separation distance. The author[4] showed that downstream injectant penetration height is directly proportional to the upstream separation distance and thus, the downstream mixing is dependent on the relative change in jet momentum. Similar conclusion for a mixing flow field was also drawn by Thayer III *et al*[5]. Weidner *et al*[6] conducted a parametric study using staged, perpendicular fuel injectors. They studied the mixing of hydrogen by varying the distance between injectors and the fuel split (percentage of fuel injected per injector). Yokota *et al*[7,8] examined the effects of injection methods, and the existence of pressure wave in the flow with the injection on mixing and total pressure loss. By the numerical investigation of two-dimensional reacting Scramjet engine flow fields, Drummond *et al*[9] found that the insufficient penetration of hydrogen caused by locating the injector 6·0cm from the engine minimum cross section reduced the overall reaction in the upstream portion of combustor. Ali *et al*[10] studied the mixing mechanisms and investigated mixing and combustion characteristics for several flow configurations. On the analysis of mixing the author observed that the backward-facing step in finite flow configuration plays an important role to enhance mixing and penetration in both upstream and downstream of injector. Investigation proved that without diffusion, injectant can spread in the flow field due to species continuity equations, but does not mix with main stream.

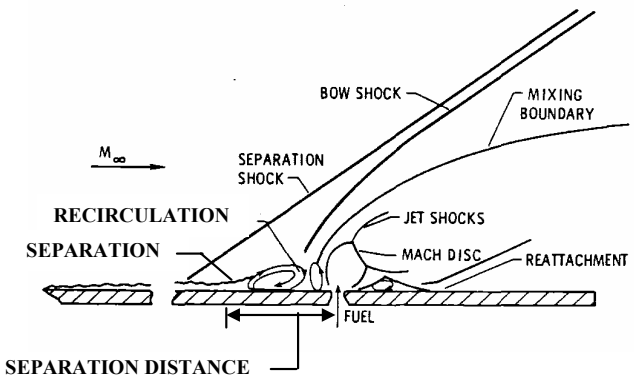


Figure 1. Flow features near fuel injector.

The geometric configuration of the calculation domain and the inlet flow conditions are shown in Fig. 2. The left boundary consists of a backward-facing step of width 5·0mm under the inlet port of air which was found efficient in mixing by Ali *et al*[11,12]. It can be pointed out that the geometry in Fig. 2 is half of an engine module in real Scramjet application and therefore the upper boundary is the symmetric line of a full engine module. To study the flow field two parameters are varied: (i) air inlet width of ranges from 6·75 ~ 27·0mm, and (ii) injection angle of ranges from 30° ~ 150°. The summary of computational runs is shown in Table 1. During the variation of inlet width, the air stream angle is taken as 90° and for the variation of injection angle, the inlet width is taken as 13·5mm since it is found the most efficient in mixing among the inlet widths. It can be pointed out that in nine cases, Cases 2 and 7 are of same configuration but for easy understanding these two cases are discussed separately in two varied parameters. For all cases the ratio of mass flow rate between air stream and injected hydrogen, and total width of the combustor remain same. The inlet conditions of air are used as Weidner *et al*[6] except Mach number. We choose the Mach 5.0 for the main flow as the test program has been conducted over the flight Mach number range[13] from 3·0 to 7·0.

https://doi.org/10.1017/S0001924000000774 Published online by Cambridge University Press

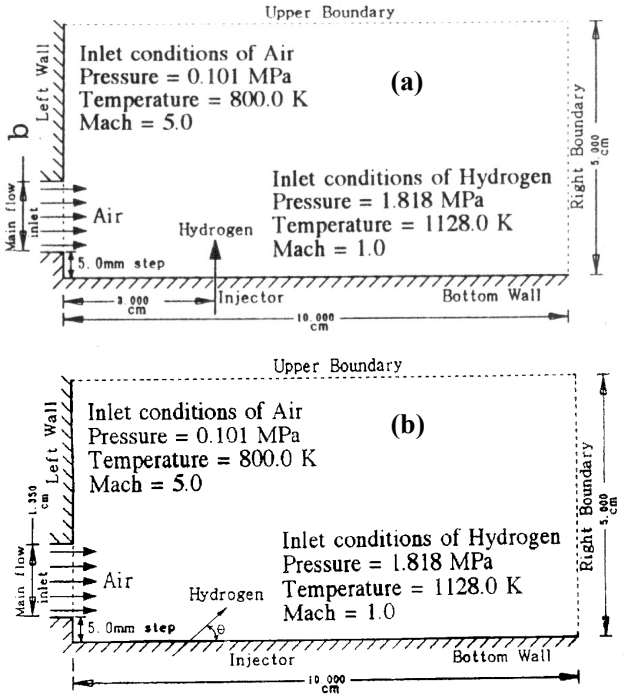


Figure 2. Schematic of the physical model, (a) different air inlet widths, and (b) different injection angles.

2.0 MATHEMATICAL MODELING

2.1 Governing equations

The flowfield is governed by the two-dimensional full Navier-Stokes equations with conservation equations of species. Body forces are neglected. For non-reacting flow, these equations can be expressed by;

$$\frac{\partial U}{\partial t}+\frac{\partial F}{\partial x}+\frac{\partial G}{\partial y}=\frac{\partial F_y}{\partial x}+\frac{\partial G_y}{\partial y} \quad \ldots (1)$$

where

$$U=\begin{pmatrix}\rho\\ \rho u\\ \rho v\\ E\\ \rho_i\end{pmatrix},\quad F=\begin{pmatrix}\rho u\\ \rho u^2+p\\ \rho uv\\ (E+p)u\\ \rho_i u\end{pmatrix},\quad G=\begin{pmatrix}\rho v\\ \rho uv\\ \rho v^2+p\\ (E+p)v\\ \rho_i v\end{pmatrix},$$

$$F_y=\begin{pmatrix}0\\ \sigma_x\\ \tau_{xy}\\ \sigma_x u+\tau_{xy}v+q_x\\ \dot{m}_{ix}\end{pmatrix},\quad F_y=\begin{pmatrix}0\\ \tau_{xy}\\ \sigma_y\\ \tau_{yx}u+\sigma_y v+q_y\\ \dot{m}_{iy}\end{pmatrix}.$$

$$P=\sum_{j=1}^{ns}\rho_j R_j T=\sum_{j=1}^{ns}\rho_j\frac{R}{W_j}T,\qquad E=\sum_{j=1}^{ns}\rho_j C_{pj}T-\sum_{j=1}^{ns}\rho_j\frac{R}{W_j}T+\frac{\rho}{2}\left(u^2+v^2\right)$$

Table 1
Summary of computational runs

Varying parameters	Computational runs (Values of parameters)		Identification
	Air inlet width, b (mm)	Injection angle, θ	
Air inlet width, b (mm)	6·75	90°	Case 1
	13·50	90°	Case 2
	20·25	90°	Case 3
	27·00	90°	Case 4
Injection angle, θ	13·50	30°	Case 5
	13·50	60°	Case 6
	13·50	90°	Case 7
	13·50	120°	Case 8
	13·50	150°	Case 9

https://doi.org/10.1017/S0001924000000774 Published online by Cambridge University Press

The following terms are expressed as,

$$\sigma_x = \lambda\left(\frac{\partial u}{\partial x}+\frac{\partial v}{\partial y}\right)+2\mu\left(\frac{\partial u}{\partial x}\right), \quad \sigma_y = \lambda\left(\frac{\partial u}{\partial x}+\frac{\partial v}{\partial y}\right)+2\mu\left(\frac{\partial v}{\partial y}\right), \quad \tau_{xy} = \tau_{yx} = \mu\left(\frac{\partial u}{\partial y}+\frac{\partial v}{\partial x}\right)$$

$$q_x = \kappa\frac{\partial T}{\partial x}+\rho\sum_{j=1}^{ns} D_j H_j \frac{\partial Y_j}{\partial x}, \quad q_y = \kappa\frac{\partial T}{\partial y}+\rho\sum_{j=1}^{ns} D_j H_j \frac{\partial Y_j}{\partial y}.$$

$$\dot{m}_{ix} = \rho D_i \frac{\partial Y_i}{\partial x}, \quad \dot{m}_{iy} = \rho D_i \frac{\partial Y_i}{\partial y}, \quad \lambda = -\frac{2}{3}\mu.$$

The values of C_p and H are considered as functions of temperature and determined from the polynomial curve fitting developed by Moss[14]. Temperature is calculated by Newton-Raphson method. The coefficients of molecular viscosity μ and thermal conductivity κ of each species are determined by Sutherland formulae and those of gas mixture by Wilke's formulae available in White[15]. The effective molecular diffusion coefficient for each species is determined by the formula given in Reid *et al*[16].

2.2 Turbulence model

A zero-equation algebraic turbulence model developed by Baldwin and Lomax[17] is used to simulate boundary layer separation, recirculation and shock-expansion regions near the injector. The model is patterned with modifications that avoid the necessity for finding the edge of the boundary layer. This has been very helpful because at the injection port and adjacent region it is difficult to define boundary layer thickness. According to the model the eddy viscosity μ_t is defined as

$$\mu_t = \begin{cases} (\mu_t)_{inner} & y \le y_{crossover} \\ (\mu_t)_{outer} & y > y_{crossover} \end{cases} \quad \ldots (2)$$

where y is the normal distance from the wall and $y_{crossover}$ is the smallest value of y at which the value of viscosity in the outer region becomes less than or equal to the value of viscosity in the inner region.

The viscosity in the inner region is given by

$$(\mu_t)_{inner} = \rho\, l^2\, |\omega| \quad \ldots (3)$$

The mixing length in the inner region l is expressed as

$$l = ky\left[1-\exp(-y^+/A^+)\right] \quad \ldots (4)$$

where

$$y^+ = \frac{\rho_w u_{\hat{o}}\, y}{\mu_w} = \frac{\sqrt{\rho_w \tau_w}\, y}{\mu_w} \quad \ldots (5)$$

For two-dimensional flow, the magnitude of the vorticity is given by

$$|\omega| = \sqrt{\left(\frac{\partial u}{\partial y}-\frac{\partial v}{\partial x}\right)^2} \quad \ldots (6)$$

For the outer region,

$$(\mu_t)_{outer} = K\, C_{CP}\, \rho\, F_{WAKE}\, F_{KLEB}(y) \quad \ldots (7)$$

where K is the Clauser constant, C_{CP} an additional constant, and

$$F_{WAKE} = \min\left\{\left(y_{max} F_{max}\right), \left(C_{wk}\, y_{max} U_{dif}^2 / F_{max}\right)\right\} \quad \ldots (8)$$

Here F_{max} is the maximum value of the function

$$F(y) = y\,|\omega|\left[1-\exp(-y^+/A^+)\right] \quad \ldots (9)$$

at each y station in the flow domain, and y_{max} is the y co-ordinate at which this maximum occurs. The function $F_{KLEB}(y)$ is the Klebanoff intermittency factor given by

$$F_{KLEB}(y) = \left[1+5\cdot5\left(\frac{C_{KLEB}\, y}{y_{max}}\right)^6\right]^{-1} \quad \ldots (10)$$

U_{dif} is the difference between the magnitude of the maximum and minimum total velocity in the profile at a fixed x station, expressed as

$$U_{dif} = \left(\sqrt{u^2+v^2}\right)_{max} - \left(\sqrt{u^2+v^2}\right)_{min} \quad \ldots (11)$$

where $\left(\sqrt{u^2+v^2}\right)$ is taken to be zero along all x station.

The outer formulation (Eqs 12 and 13) can be used in wakes as well as in attached and separated boundary layer. The product $y_{max}F_{max}$ replaces $\delta^* u_e$ in the Clauser formulation and the combination $y_{max}U_{dif}^2/F_{max}$ replaces U_{dif} in a wake formulation. In effect, the distribution of vorticity is used to determine length scales so that the necessity for finding the outer edge of the boundary layer is removed.

The following are the constants used for this model and are directly taken from Baldwin and Lomax[17]:

$A+ = 26$,	$C_{CP} = 1{\cdot}6$,	$C_{KLEB} = 0{\cdot}3$,
$C_{wk} = 0{\cdot}25$,	$k = 0{\cdot}4$,	K = 0.0168

The values of the turbulent thermal conductivity of the mixture κ_t and turbulent diffusion coefficient of i-th species D_{it} are obtained from eddy viscosity coefficient μ_t by assuming a constant turbulent Prandtl and Lewis number equal to 0·91 and 1·0, respectively. They can be expressed as

$$\frac{\mu_t Cp}{k_t} = 0{\cdot}91 \quad \ldots (12)$$

$$\frac{\rho\, D_{it} Cp}{k_t} = 1{\cdot}0 \quad \ldots (13)$$

The final values of μ, κ and D_{im} used in the governing equations are

$$\mu = \mu_l + \mu_t \quad \ldots (14)$$

$$\kappa = \kappa_l + \kappa_t \quad \ldots (15)$$

https://doi.org/10.1017/S0001924000000774 Published online by Cambridge University Press

$$D_{im} = D_{iml} + D_{it} \quad \ldots (16)$$

2.3 Numerical scheme

The system of governing equations is solved using an explicit Harten-Yee Non-MUSCL Modified-flux-type TVD scheme[18]. The two-dimensional, rectangular physical co-ordinate system(x, y) is transformed into the computational co-ordinate system (ξ, η) in order to solve the problem on uniform grids. After applying the transformation, Equation (1) can be expressed as:

$$\frac{\partial \hat{U}}{\partial t} + \frac{\partial \hat{F}}{\partial \xi} + \frac{\partial \hat{G}}{\partial \eta} = \frac{\partial \hat{F}_v}{\partial \xi} + \frac{\partial \hat{G}_v}{\partial \eta} \quad \ldots (17)$$

where $\hat{U} = J^{-1}U$, $\hat{F} = J^{-1}(\xi_x F + \xi_y G)$, $\hat{G} = J^{-1}(\eta_x F + \eta_y G)$

$\hat{F}_v = J^{-1}(\xi_x F_v + \xi_y G_v)$, $\hat{G}_v = J^{-1}(\eta_x F_v + \eta_y G_v)$.

The grid Jacobian J and metric terms are, $J^{-1} = x_\xi y_\eta - x_\eta y_\xi$,

$\xi_x = J y_\eta$, $\xi_y = -J x_\eta$, $\eta_x = -J y_\xi$, $\eta_y = J_\xi$.

For the left hand side of Equation (17), the explicit Non-MUSCL TVD scheme can be written as

$$\hat{U}_{i,j}^{n+1} = \hat{U}_{i,j}^{n} - J_{i,j}\frac{\Delta t}{\Delta \xi}\left(\hat{F}_{i+1/2,j}^{n} - \hat{F}_{i-1/2,j}^{n}\right) - J_{i,j}\frac{\Delta t}{\Delta \eta}\left(\hat{G}_{i,j+1/2}^{n} - \hat{G}_{i,j-1/2}^{n}\right) \quad \ldots (18)$$

The variables $\hat{F}$ and $\hat{G}$ can be described as

$$\hat{F}_{i+1/2,j}^{n} = \frac{1}{2}\left(\hat{F}_{i,j}^{n} + \hat{F}_{i+1,j}^{n} + \hat{R}_{i+1/2}\,\hat{\Phi}_{i+1/2}\right) \quad \ldots (19)$$

The $\hat{R}_{i+1/2}$ is an eigen vector matrix and $\hat{\Phi}_{i+1/2}$ is a vector with the elements $\phi^l_{i+1/2}$ (l = 1, 2, 3, 4, 5). The variables used in the above equations are

$$\hat{\Phi}_{i+1/2} = \left\{\hat{\Phi}^l{}_{i+1/2}\right\} = \left\{\sigma\left(\hat{a}^l{}_{i+1/2}\right)\left(\hat{g}^l{}_{i+1} + \hat{g}^l{}_{i}\right) - \psi\left(\hat{a}^l{}_{i+1/2} + \hat{\gamma}^l{}_{i+1/2}\right)\hat{\alpha}^l{}_{i+1/2}\right\};$$

$$l = 1\sim5. \quad \ldots (20)$$

$$\sigma(z) = \frac{1}{2}\left\{\psi(z) - \frac{\Delta t}{\Delta \xi}z^2\right\} \quad \ldots (21)$$

$$\psi(z) = \begin{cases} z & ; \quad |z| \geq \delta_l \\ (z^2 + \delta_l^2)/2\delta_l & ; \quad |z| < \delta_l \end{cases} \quad \ldots (22)$$

δ_l is a function that defines the range of entropy correction, and should be a function of the contravariant velocity and the corresponding sound speed for the computations. The form of the function used here is

$$\delta_l = \bar{\delta}\left(|U| + |V| + c\sqrt{\xi_x^2 + \xi_y^2 + \eta_x^2 + \eta_y^2}\right) \quad \ldots (23)$$

with a constant $\bar{\delta}$ set to 0·15. More details about the scheme can be found in Yee[19].

The minmod limiter, simplified form of which can be found in Yee[19], was used to avoid the numerical oscillations at the discontinuity. Among the various approximate Riemann solvers[19], we used the Roe's average which is the most common one due to its simplicity and ability to return to the exact solution whenever the variables lie on a shock or contact discontinuity.

3.0 BOUNDARY CONDITIONS AND CONVERGENCE CRITERION

A Navier-Stokes analysis imposes that the normal and tangential velocity components are zero on the walls. The walls are assumed to be thermally adiabatic, so that $(\partial T/\partial n)_w = 0$. For non-catalytic walls, the normal derivative of species mass fraction also vanishes, and consequently the gradient of total density becomes zero. The pressure is determined from the equation of state. The temperature, pressure and density at inflow boundary are assumed steady. At outflow boundary the variables are determined by first-order extrapolation due to supersonic character of flow. Throughout the present study, the following convergence criterion has been set on the variation of density:

$$\sqrt{\frac{\sum_{J=1,K=1}^{JJ,KK}\left(\frac{\rho_{new} - \rho_{old}}{\rho_{old}}\right)^2}{JJ.KK}} \leq 10^{-5} \quad ,$$

where JJ and KK are the total number of nodes in the horizontal and vertical directions, respectively.

4.0 RESULTS AND DISCUSSION

4.1 Program verification

To verify the present code, a comparison has been made with the experimental data published by Weidner *et al*[6]. The geometry of the experiment is shown in the inset on Fig. 3, where helium was injected at sonic condition from a 0·0559 cm slot into a rectangular duct of 25·4 cm long and 7·62cm high. The slot was located 17·8cm downstream of the duct entrance. The flow conditions of helium at the slot exit were P = 1·24MPa, T = 217·0K and M = 1·0. At the entrance of the duct, the airstream conditions were P = 0·0663MPa, T = 108·0K and M = 2·9. Using the same geometry and flow conditions we computed the flowfield with a grid system consisting of 246 × 165 nodes in the horizontal and vertical directions, respectively. At the exit of the injector ten nodal points are used.

Results are given in Figs. 3-5. Figure 3 shows that the computed pressure along the bottom wall agrees well with the experiment in both the upstream and downstream of the injector. Both show a pressure rise in the upstream separated region and downstream reattachment region. An over-prediction can be found at the immediate downstream of the injector where the turbulence is naturally intensified by the disturbance caused by the injector. Figure 4 gives the

https://doi.org/10.1017/S0001924000000774 Published online by Cambridge University Press

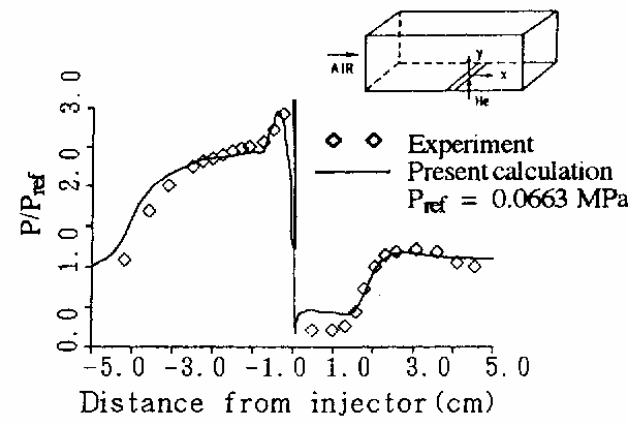


Figure 3. Comparison between experimental and computed pressures along bottom wall.

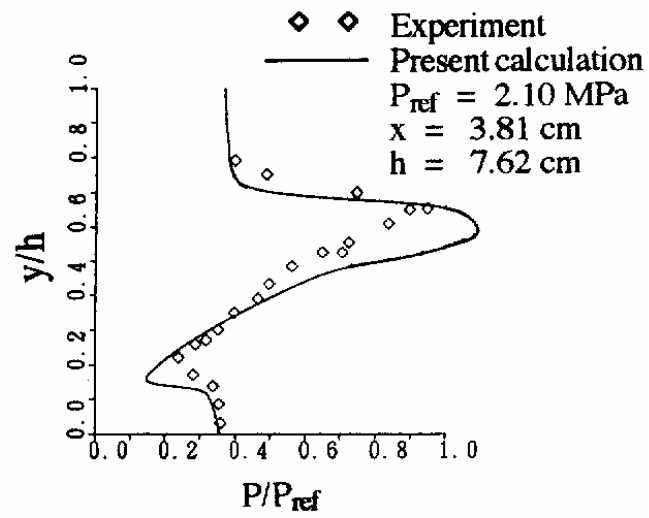


Figure 4. Comparison between experimental and computed pressures at 3·81 cm downstream of injector.

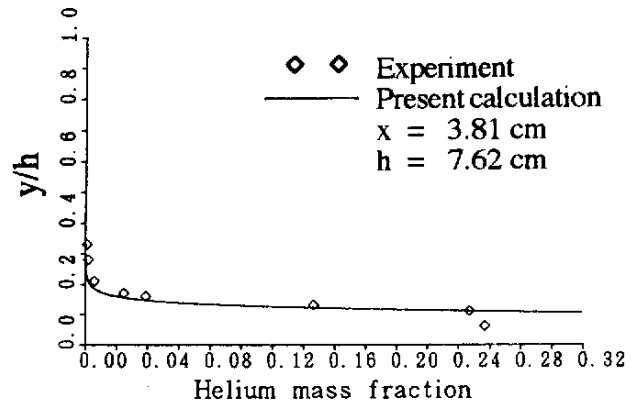


Figure 5. Comparison among helium mass fraction at 3·81 cm downstream of injector.

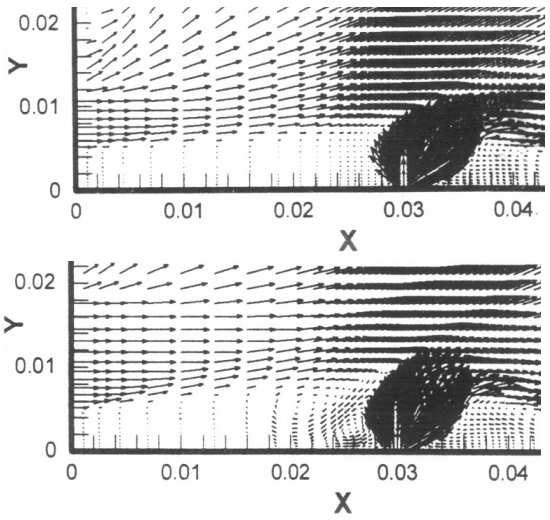


Figure 6. Velocity vector around the injector; (a) Case 1, and (b) Case 2.

static pressure distribution along the vertical axis at 3·81cm downstream of the injector. Qualitatively, the computed pressure profile agrees with the experimental data. Small variation on the position of recompression shock and bow shock, and the pressures at these positions can be observed in the computation. In the experiment, the recompression shock occurs at y/h = 0·2 (h is the height of domain), whereas in computation at 0·16. After recompression, both show a linear increase of pressure. The calculation determines the similar difference in the position of bow shock as that of recompression shock. In the experiment the position of bow shock is at y/h = 0·63, while in computation it is 0·59. Beyond the bow shock, the calculation shows the similar decreasing rate of pressure with experiment. Figure 5 shows the comparison between the mass fraction profiles of injected helium along the same vertical axis at 3·81cm downstream of the injector. The computed curve agrees with the experimental data at all points along the vertical axis.

The computation shows that the overall computed results agree with the experiment in spite of the complexities of injected flowfield. The code is therefore considered to be adequate for application to calculate the mixing flowfields.

4.2 Effect of air inlet width

The velocity in upstream of injector, penetration and diffusion of hydrogen, and mixing efficiencies of different cases have been analyzed and discussed. In figures X and Y denote the distance in meter from left boundary and bottom wall, respectively. Figure 6 shows the velocity vector in upstream recirculation region for Case 1 and 2. It can be pointed out that upstream recirculation plays an important role to increase the mixing for high Mach number as described by Ali *et al* [10]. In Fig. 6(b) we can see that there is one primary large recirculation elongated up to backward-facing step. Immediate upstream of injector one secondary recirculation is evolved caused by primary recirculation and suction of side jet. Due to these recirculations hydrogen reaches up to backward-facing step with high concentration by convection and diffusion mechanisms. On the other hand, no recirculation in upstream can be found in Fig. 6(a), rather the flow in the region between backward-facing step and injector is seemed to be stagnant. Therefore, the mixing in this region is dominated by diffusion only. The velocity vectors in upstream of Case 3 and 4 are similar to Case 2 and are not shown here. However, the outcome can be found in Fig. 7, which shows the penetration and mass concentration of

https://doi.org/10.1017/S0001924000000774 Published online by Cambridge University Press

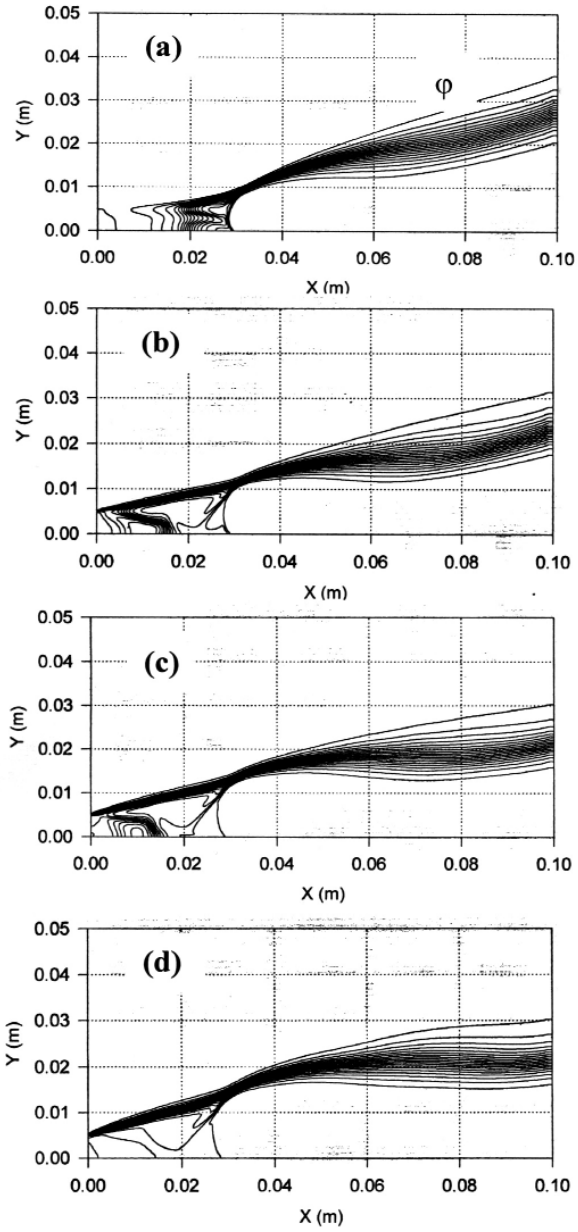


Figure 7. Mole fraction contours of hydrogen, φ = contour levels ranges from 0·05~0·95 with an increment of 0·05; (a) Case 1, (b) Case 2, (c) Case 3, and (d) Case 4.

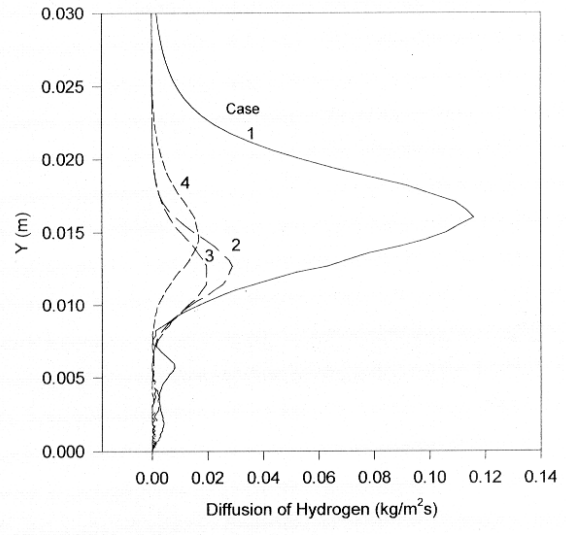


Figure 8. Diffusion of hydrogen at 0·076m of *X* location (Case 1~4).

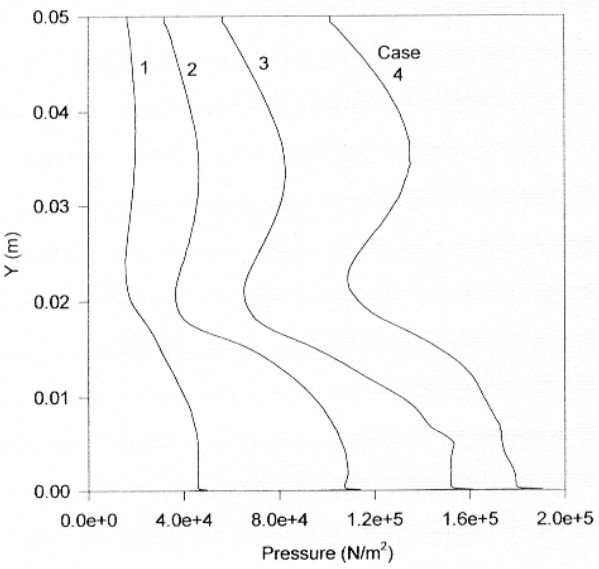


Figure 9. Pressure distribution at 0·076m of *X* location (Case 1~4).

hydrogen in both upstream and downstream of injector. There are various definitions of 'penetration' in the literature. In this paper the term 'penetration' is referred to the edge of mixing region in the vertical direction where the mole fraction of hydrogen is 5%. Figure 7(a) shows very low concentration of hydrogen close to backward-facing step. In Case 1 due to small inlet width, air expands and fills up the space between step and injector and consequently only a small amount of hydrogen reaches to facing step by diffusion. On the other hand, higher mass flow rate of hydrogen, their expansion and strong interaction with air cause primary and secondary recirculations and eventually higher diffusion and better mixing occur in Cases 2~4. This trend is continued the whole upstream region. Though for all cases the pattern of mole fraction contours of hydrogen are similar at the top of injector, the penetration height increases with the increase of inlet width caused by strong interaction and higher concentration of hydrogen. At far downstream the slope of mole fraction contours decreases with the increase of inlet width. It has two reasons: (i) with the increase of inlet width the momentum of mainflow increases. Though the momentum of side jet is increased proportionately, strong interaction of air stream weakens and bends the hydrogen jet and eventually the slope decreases, and (ii) in downstream diffusion of hydrogen decreases with the increase of inlet width as shown in Fig. 8. This is quite natural because for wider inlet, mass flow rate of both air and hydrogen increases the pressure in the flow field as shown in Fig. 9 resulting in decrease of expansion as well as diffusion of hydrogen.

https://doi.org/10.1017/S0001924000000774 Published online by Cambridge University Press

The performance of different cases is evaluated by calculating mixing efficiency. Mathematically, the mixing efficiency is defined by

$$\eta_m = \frac{\int_A \left(f_H \rho \vec{u} \, d\vec{A}\right) / \phi'}{\dot{m}_H / \Phi}$$

where,

A = arbitrary section plane
f_H = local mass fraction of hydrogen
ρ = total density
$\vec{u}$ = velocity vector
$d\vec{A}$ = small area normal to velocity vector
$\dot{m}_H$ = total mass flux of hydrogen
ϕ' = local equivalence ratio = $\begin{cases} 0{\cdot}25 & \phi' < 0{\cdot}25 \\ \phi' & \phi' \geq 0{\cdot}25 \end{cases}$

Physically mixing efficiency indicates the ratio of hydrogen mass flow rate capable of burning to its total mass flow rate at the exit of side jet. In the flow field where large amount of hydrogen is present with negligible amount of oxygen, the calculation of mixing efficiency is avoided by dividing the large value of ϕ'. On the other hand, where a very small amount of hydrogen is present, an error in calculation of mixing efficiency can be occurred by the small value of ϕ'. This error has been eliminated by setting the minimum value of $\phi' = 0{\cdot}25$ which corresponds to the lower flammability limit. It can be mentioned that Yokota *et al*.[7,8] used similar expression for calculating mixing efficiency in the flow field. In this investigation, the global equivalence ratio for all cases is $\Phi = 2$. The mixing efficiency along the combustor length is shown in Fig. 10. To analyze the mixing, the calculation domain is divided into three regions; (i) upstream, (ii) injection, and (iii) downstream region. In upstream due to recirculation in Case 2~4 hydrogen mixes up well with air resulting in increase of mixing efficiency. On the other hand, in Case 1 hydrogen can not mix well with air due to absence of recirculation resulting in decrease of mixing. Around the injector, the rate of increasing the mixing with length is high in Case 1 caused by expansion and diffusion of hydrogen (shown in Fig. 8) due to lower flow field pressure (shown in Fig. 9), while in other cases, diffusion and mixing decrease with the increase of inlet width. At far downstream mixing is dominated by diffusion. Due to high pressure and supersonic nature of flow, the diffusion as well as mixing in Cases 2~4 is very small, while in Case 1 considerably higher diffusion and mixing are occurring, though it can not recover the deficiency of mixing occurred in upstream. By the combination of all these effects discussed above, Case 2 shows the highest mixing efficiency among the Cases 1~4. It can be pointed out that though the penetration of hydrogen at right boundary is maximum in Case 1 as shown in Fig. 7(a), the mixing efficiency decreases which indicates that higher penetration of hydrogen does not always mean the larger mixing efficiency. The general trend of mixing efficiency with the main flow inlet width is that the mixing efficiency increases with the increase of inlet width up to 13·5mm and then decreases.

4.3 Effects of injection angle

Figures 11 (a~e) show the velocity vector in both upstream and downstream of injector. A pair of recirculation regions formed at the upstream of the injector, one of which is large and the other is small in size. In case 5 the recirculations are weak, which can be understood by the vector length in recirculation region. The increase of injection angle makes the recirculations stronger which can be found

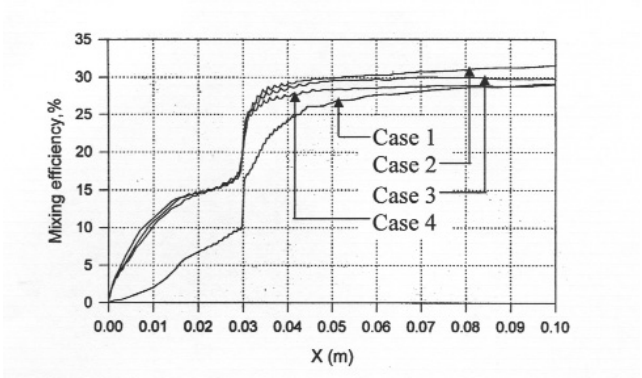


Figure 10. Mixing efficiency along the length of physical model (Case 1~4).

in cases 6 and 7. For further increase of injecting angle i.e. in cases 8 and 9 they are not significant. The large primary clockwise recirculation is caused by the backward facing step and the secondary small counter-clockwise recirculation close to injector is caused by the primary recirculation and the suction of injection. The primary recirculation increases the boundary layer thickness and the injection into a thick boundary layer causes greater penetration resulting in higher mixing. Due to interaction between main flow and side jet, the velocity of main flow decreases and the air enters the upstream recirculation. On the other hand, by diffusion and convection due to injection, the injected hydrogen enters the recirculation and mixes well with air. So upstream recirculations play a vital role on mixing and consequently cases 7 and 8 show better mixing. Downstream there is no strong recirculation in any case. Case 7 shows a very small recirculation just downstream of the injector caused by the suction of the injection and bending of the side jet. This recirculation and convection due to injection cause better mixing in case 7.

Figures 12(a~e) show the penetration and mass concentration of hydrogen in the flow field. It can be pointed out that the penetration and mixing of hydrogen in a numerical simulation can occur by means of (i) turbulence and convection due to recirculation, and (ii) molecular diffusion. The backward facing step associated with upstream recirculation brings the injected hydrogen up to the left boundary in all cases. The hydrogen penetration height at different downstream locations can be compared from Figs. 12(a~e). For example, at 10cm from left boundary the penetration height is up to 2 cm in case 5, whereas, it is 2·5cm for case 6 and above 3cm for cases 7 and 8. The penetration height of the hydrogen is higher in cases 7 and 8 (above 3cm) indicating more uniform distribution of hydrogen and consequently higher mixing efficiency. In Figs. 12(a~e) φ indicates the contour level of hydrogen mole fraction. The value of the minimum contour level is 0·05 and that of the maximum contour level is 1·0. The increment of adjacent higher contour level is 0·05. For all cases (case 5~9) the mole fraction contours of hydrogen are concentrated in a narrow region on the top of the injector, as shown in Figs. 12(a~e), which might become a high heat release zone in the reacting flowfield. The flame holding requires longer residence time of flame in the burning range and this residence time strongly depends on the geometric expansion of the recirculation zone[20]. Also the equivalence ratio of fuel and oxidizer in mixture is an important factor for burning because among the mixtures, the stoichiometric mixture strength is good for combustion. Therefore, longer recirculation zone containing stoichiometric mixture strength results in a longer residence time and leads to a more stable flame. Accordingly cases 7 ($\theta = 90°$) and 8 ($\theta = 120°$) have good flame holding capability, because they can produce larger and elongated upstream recirculation where most of the region contains good proportion of hydrogen and oxygen. Again in cases having $\theta = 30°$ and 150° upstream region contains lower mass cencentration of hydrogen

https://doi.org/10.1017/S0001924000000774 Published online by Cambridge University Press

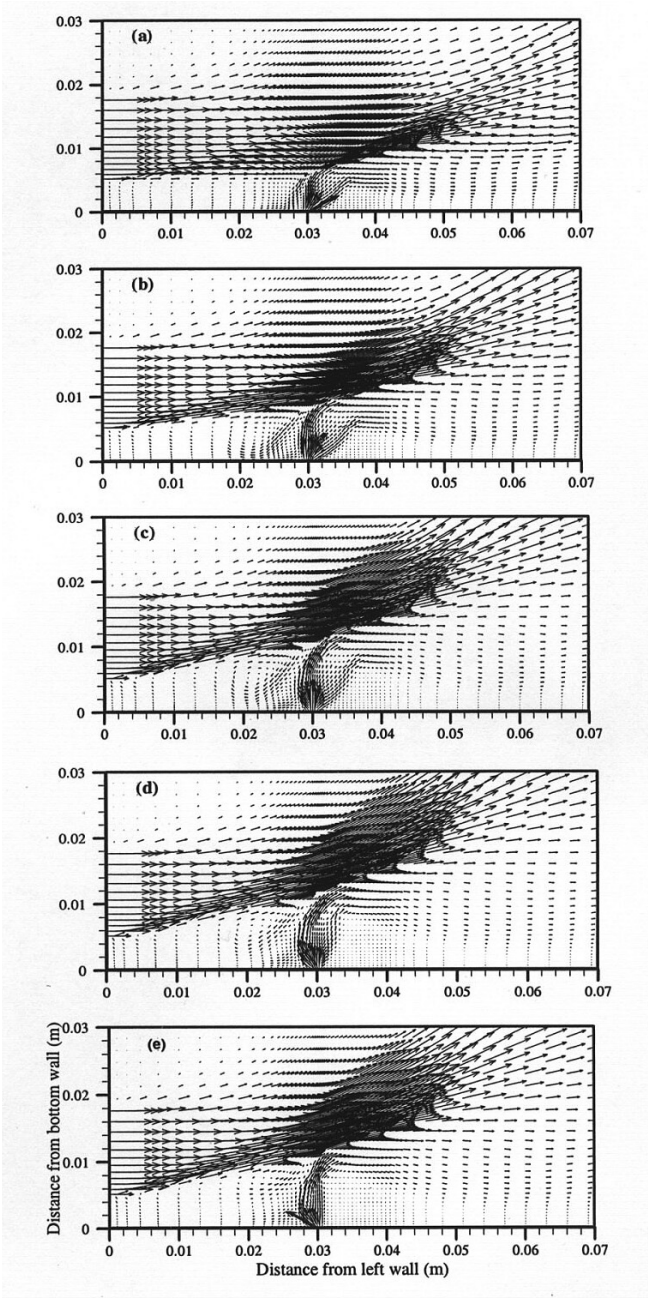


Figure 11. Velocity vector near injector; (a) Case 5, (b) Case 6, (c) Case 7, (d) Case 8, and (e) Case 9.

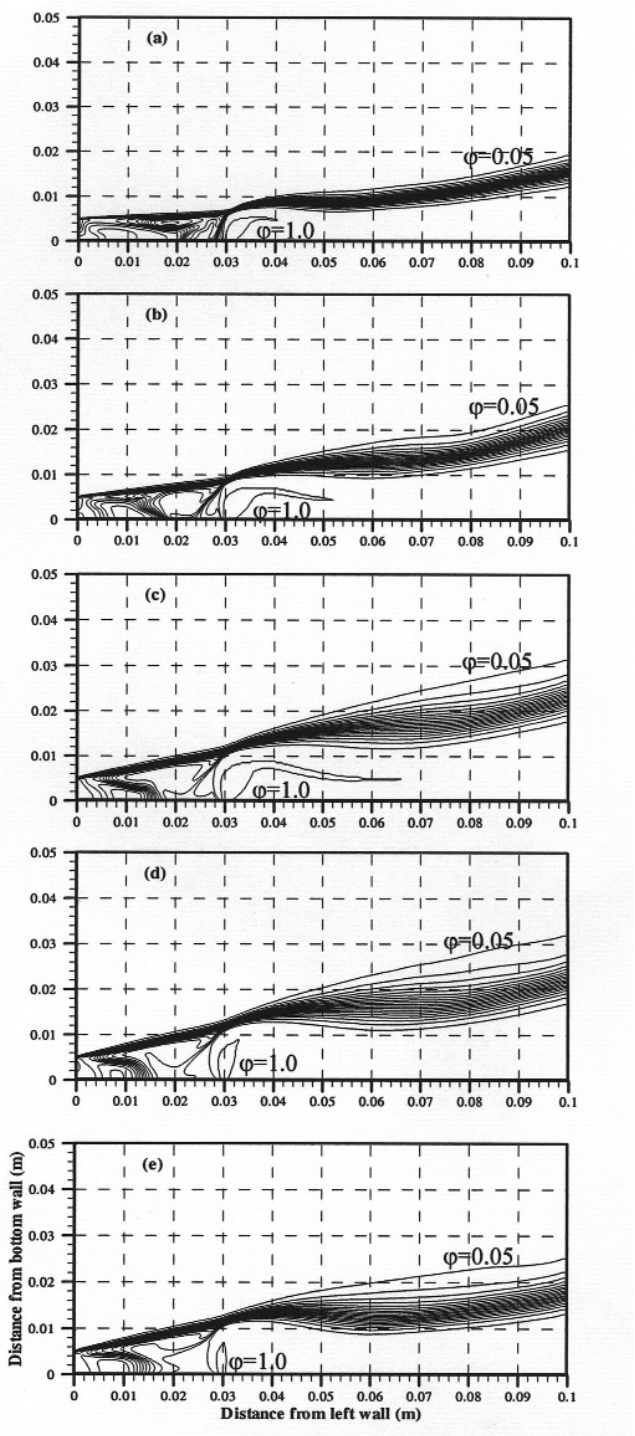


Figure 12. Mole fraction contour of Hydrogen, φ (0·05, 1·0); φ is contour level, (a) Case 5, (b) Case 6, (c) Case 7, (d) Case 8, and (e) Case 9.

which is not good for flame holding. In downstream hydrogen distribution is seemed to be better in cases 7 and 8 as mentioned earlier because of higher expansion of side jet.

The performance of different cases is evaluated by calculating mixing efficiency. Figure 13 shows that mixing efficiency increases sharply at injector position caused by high mass concentration of hydrogen. In general, the increasing of mixing is moderate in upstream region and in downstream it is very slow. Individually, case 7 ($\theta = 90°$) and case 8 ($\theta = 120°$) have the highest value of mixing efficiency (28%) at injector position due to strong upstream recirculation. In downstream the increasing rate of mixing along the length of physical model for case 7 ($\theta = 90°$) is higher than case 8 ($\theta = 120°$), whereas, for case 9 ($\theta = 150°$) it remains almost constant which indicates that very long combustor might increase the construction cost for case 9 provided the other parameters are identical. Among the cases considered in this investigation two competing phenomena about the mixing can be observed: i) in upstream mixing is dominated by recirculation and ii) in downstream it is dominated by hydrogen mass concentration. Due to larger recirculation in upstream of injector hydrogen mixes well with oxygen in cases 7~9 indicating higher mixing efficiency. In downstream cases 5 and 6

https://doi.org/10.1017/S0001924000000774 Published online by Cambridge University Press

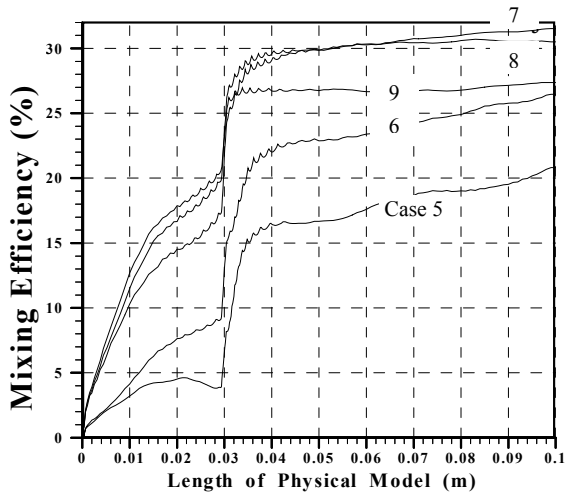


Figure 13: Mixing efficiency along the length of physical model (Case 5~9).

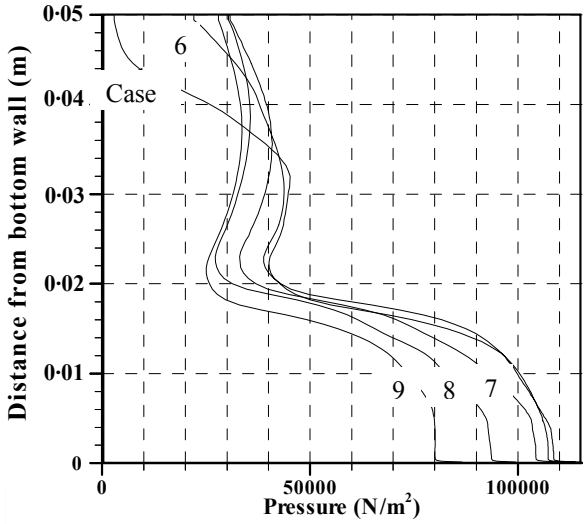


Figure 14. Pressure distribution at 0.076m from left wall (Case 5~9)

show higher increasing rate of mixing due to higher mass concentration of hydrogen. However, mixing efficiency increased by recirculation in cases 7~9 can not be recovered in cases 5 and 6 by increasing rate of mixing efficiency dominated by hydrogen mass concentration in downstream. Finally, we can see that case 7 shows the maximum mixing efficiency (31·5%) at the right end of calculation domain.

The characteristics of the flow field of cases 5~9 are shown in Figs 14 and 15(a~e). Figure 14 shows the pressure distribution along the axis at 0·076 m from left wall. In general, pressure in downstream near the bottom wall is highest for all cases. Along vertical direction the pressure decreases up to the domain height of 2·0cm. Above that height the pressure remains constant in cases 7~9, whereas, in cases 5 and 6 the pressure decreases near the upper boundary of the domain. Another observation is that with the increase of injection angle pressure decreases in downstream except at the upper part. This is caused by the weaker reattachment shock in downstream when injection angle is increased. Due to strong suppression of side jet in cases 5 and 6 caused by the high momentum of main flow the reattachment shock becomes stronger resulting in higher pressure in downstream. As diffusion of hydrogen is inversely proportional to the pressure, therefore, lower value of pressure indicates higher diffusion at downstream which results in greater mixing rate for the cases of higher injection angle. Figure 15(a~e) shows the pressure contours by which the pressure distribution and different shocks can be understood. Flow separation is initiated by the backward facing step at left boundary. The main flow is deflected upward by the existance of wall at the upper part of the left boundary and the momentum of injecting flow along upward direction. The deflection angle first increases with the increase of injection angle and then decreases for further increase of injection angle. Therefore, the deflection angle of main flow is maximum for case 7 (θ =90°) caused by the interaction of main flow with the highest momentum of injecting flow. It can be pointed out that the momentum of the injecting flow along the upward direction is maximum when the injection angle is 90° i. e. case 7. The under expanded side jet rapidly expands and forms a Mach disk and a bow shock due to the interaction with main flow. For the injection angle θ =90° the slope of the bow shock is steeper indicating high iteraction between the main flow and side jet. Strong interaction causes high penetration and more uniform mixing of hydrogen in downstream. The maximum pressure and temperature in the flow field have been found immediately behind the intersection of separation shock and bow shock. In the downstream region the reattachement shock is more visible which starts almost at the same position of the bottom wall for all cases. The pressure is higher in the upstream recirculation region while it is much lower immediately behind the injector caused by the suction of injection.

5.0 CONCLUSIONS

A numerical study on supersonic mixing of hydrogen with air has been performed for the four inlet widths of airstream and five injection angles. When air inlet widths were varied, it was found that the expansion of air stream was high for the smallest inlet width resulting in small upstream recirculation as well as low mixing efficiency. Though the increment of mixing for the smallest width was highest in downstream, it could not recover the deficiency of mixing occurred in upstream resulting in lower mixing efficiency. For the variation of injection angle, two competing phenomena were observed: i) in upstream of injector mixing efficiency was dominated by convection due to recirculation and ii) in downstream mixing efficiency was dominated by mass concentration of hydrogen. Incorporating all the effects the configuration of injection angle 90° and medium inlet width of air stream (13·5mm) had the maximum mixing efficiency and its upstream recirculation region with good proportion of hydrogen and oxygen might act as a good flame holder in Scramjet combustor. For the injection angle θ = 90° the slope of the bow shock is steeper indicating high interaction between the main flow and side jet. Strong interaction causes high penetration and more uniform mixing of hydrogen in downstream.

REFERENCES

1. BROWN, G.L. and ROSHKO, A. On density effects and large structure in turbulent mixing layer, 1974, *J Fluid Mech,* **64,** (4), pp 575-816.
2. PAPAMOSCHOU, D. and ROSHKO, A. Observation of supersonic free shear layers, 1986, AIAA Paper, 86-0162.
3. ROGERS, R.C. A study of the mixing of hydrogen injected normal to a supersonic airstream, 1971, NASA TN, D-6114.
4. KRAEMER, G.O. and TIWARI, S.N. Interaction of two-dimensional transverse jet with a supersonic mainstream, 1983, NASA CR, 175446.
5. THAYER W.J. and CORLETT, R.C. Gas dynamic and transport phenomena in the two-dimensional jet interaction flow field, *AIAA J,* 1972, **10,** pp 488-493.
6. WEIDNER, E.H. and DRUMMOND, J.P. A parametric study of staged fuel injector configurations for scramjet applications, 1981, AIAA Paper 81-11468.

https://doi.org/10.1017/S0001924000000774 Published online by Cambridge University Press

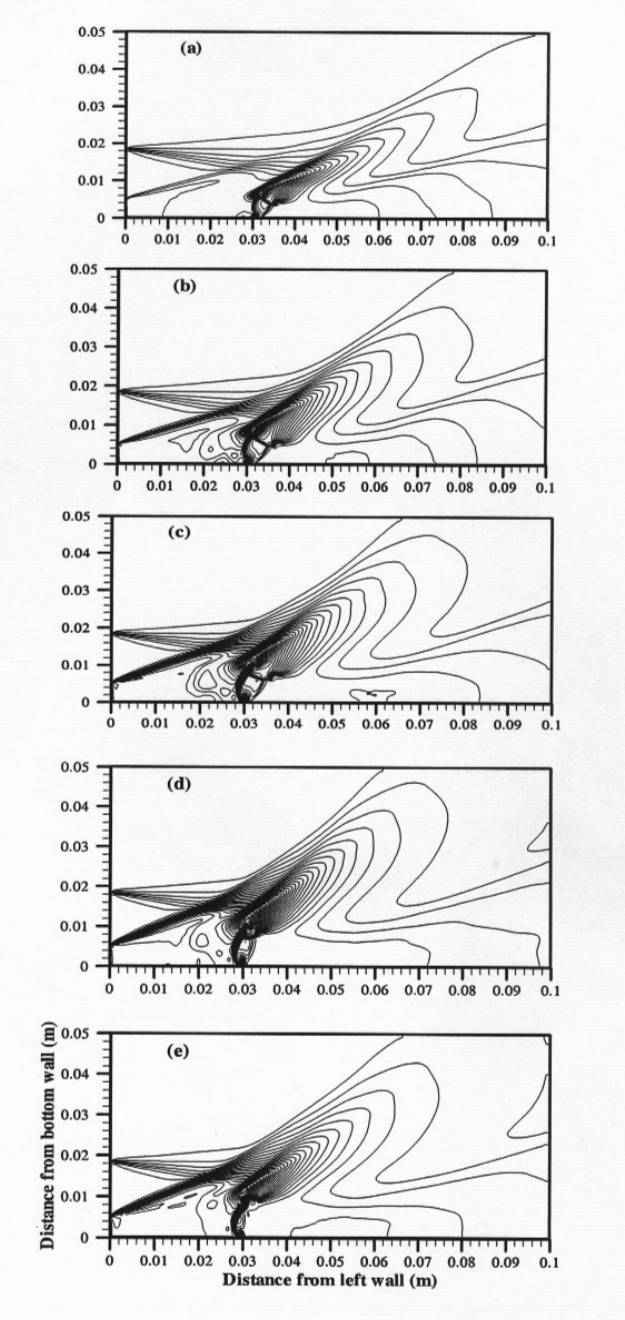


Figure 15. Pressure (N/m^2) contour, (2*104, 2*106, 2*104), φ is contour level; (a) Case 5, (b) Case 6, (c) Case 7, (d) Case 8, and (e) Case 9.

7. YOKOTA, K. and KAJI, S. The three-dimensional supersonic flow and mixing fields with a perpendicular air injection from a finite length slit, Trans. *Japan Soc Aero Space Sci,* 1996, **39,** (124), pp 173-183.
8. YOKOTA, K. and KAJI, S. The effects of aspect ratio of a finite length slit on the mixing in the three-dimensional supersonic flow, Trans. *Japan Soc Aero Space Sci*, 1996, **39,** (124), pp 199-210.
9. DRUMMOND, J.P. and WEIDNER, E.H. Numerical study of a scramjet engine flow field, January 1981, AIAA Paper, 81-0186.
10. ALI, M., FUJIWARA, T. and LEBLANC, J.E. Influence of main flow configuration on mixing and flameholding in transverse injection into supersonic airstream, 2000, *Int J Eng Sci,* **38,** pp 1161-1180.
11. ALI, M., FUJIWARA, T. and LEBLANC, J.E. The effects of backward-facing step on mixing and flame holding in supersonic combustor, 2001, *J Energy, Heat & Mass Trans,* **23,** pp 319-338.
12. ALI, M. and FUJIWARA, T. Penetration and mixing of hydrogen injected normal to a 2-Dimensional parallel supersonic flow, 1997, Trans. *Japan Soc Aero Space Sci,* **40** (130), pp 248-261.
13. RAUSCH, V.L., MCCLINTON, C.R. and HICKS, J.W. Scramjet breath ew life into hypersonics, July 1997, *Aerospace America,* pp 40-46.
14. MOSS, J.N. Reacting viscous-shock-layer solutions with multicomponent diffusion and mass injection, NASA TR, 411, 1974.
15. WHITE, F.M. *Viscous Fluid Flow,* 1974, McGraw-Hill, New York.
16. REID, R.C. and SHERWOOD, T.K. *The Properties of Gases and Liquids,* 1966, Second Edition, McGraw-Hill, New York, pp 520-543.
17. BALDWIN, B.S. and LOMAX, H. Thin layer approximation and algebraic model for separated turbulent flows, 1978, AIAA Paper, 78-257.
18. YEE, H.C. A class of high-resolution explicit and implicit shock capturing methods, 1989, NASA TM, 101088.
19. YEE, H.C. Upwind and symmetric shock-capturing schemes, December 1990, NASA TM, 89464.
20. TABEJAMAAT, S.J.U.Y. and NIIOKA, T. Numerical simulation of secondary combustion of hydrogen injected from preburner into supersonic airflow, *AIAA J,* 1997, **35,** (9), pp 1441-1447.

https://doi.org/10.1017/S0001924000000774 Published online by Cambridge University Press